Conformal Dual-Band Near-Perfectly Absorbing Mid-Infrared Metamaterial Coating

Zhi Hao Jiang,[†] Seokho Yun,[†] Fatima Toor,[‡] Douglas H. Werner,* and Theresa S. Mayer*

Department of Electrical Engineering, The Pennsylvania State University, University Park, Pennsylvania 16802, United States. [†]These authors contributed equally to this work. [‡] Current address: Silicon Materials and Devices, National Renewable Energy Lab, Golden, Colorado, 80401, United States.

O ptical metamaterials[1,2] are composite structures composed of nanoscale resonators organized to give a highly customized electric and magnetic response over a specific wavelength range of interest. Most of the revolutionary new optical devices that are being enabled by the unique effective medium properties of the metamaterial require a negative, zero, or graded refractive index with extremely low absorption loss. Several prominent device examples that exploit these properties include perfect lenses,[3,4] flat collimating lenses,[5] and invisibility cloaks.[6,7] Another far less studied class of metamaterials relies on creating structures that are tailored for complete absorption of the incident light in one or more wavelength bands independent of polarization and incidence angle.[8,9] Thus metamaterial absorber (MMA) designs must balance the electric and magnetic resonances within each wavelength band to simultaneously minimize reflection and transmission and, hence, maximize absorption for both the incident electric and magnetic fields. The availability of such MMAs could provide significant performance improvements for diverse applications including microwave-to-infrared signature control,[8−11] biochemical spectroscopy,[12−19] and thermal imaging.[20−22]

Rapid progress has been made in demonstrating MMAs that operate in the microwave and terahertz (up to 1.6 THz) regimes.[8−17] A number of single-band device designs were reported with measured polarization-independent absorptivity greater than 90% for angles of incidence from 0° to 60° at frequencies up to 1.6 THz.[10,12] More advanced multiband terahertz MMAs with up to three well-defined absorption bands have also been designed and fabricated.[14−16] Currently, the best performing dual-band MMA has a

ABSTRACT Metamaterials offer a new approach to create surface coatings with highly customizable electromagnetic absorption from the microwave to the optical regimes. Thus far, efficient metamaterial absorbers have been demonstrated at microwave frequencies, with recent efforts aimed at much shorter terahertz and infrared wavelengths. The present infrared absorbers have been constructed from arrays of nanoscale metal resonators with simple circular or cross-shaped geometries, which provide a single band response. In this paper, we demonstrate a conformal metamaterial absorber with a narrow band, polarization-independent absorptivity of >90% over a wide ±50° angular range centered at mid-infrared wavelengths of 3.3 and 3.9 μm. The highly efficient dual-band metamaterial was realized by using a genetic algorithm to identify an array of H-shaped nanoresonators with an effective electric and magnetic response that maximizes absorption in each wavelength band when patterned on a flexible Kapton and Au thin film substrate stack. This conformal metamaterial absorber maintains its absorption properties when integrated onto curved surfaces of arbitrary materials, making it attractive for advanced coatings that suppress the infrared reflection from the protected surface.

KEYWORDS: mid-infrared · conformal · metamaterial · multiband · absorber · reflection suppression · nanoresonator

maximum absorptivity of 85% at 1.41 THz and 94% at 3.02 THz measured at a 30° incidence angle.[15] Several of the terahertz devices incorporated a flexible Kapton film as the dielectric spacer to enable their use in conformal coatings.[12,14] A new type of absorber with a 2D omnidirectional broadband response[11] was designed using transformation electromagnetics approaches.[23]

Fewer high-performance infrared-to-visible MMAs have been experimentally verified because the aggressively scaled nanoresonators needed to reach these shorter wavelengths impose even stricter constraints on the metamaterial design and fabrication process.[18,22] Recently, an angularly tolerant single-band MMA designed for near-IR operation at 1.6 μm was implemented by patterning a periodic array of simple circular Au features on a planar magnesium difluoride and Au thin film stack.[18] The absorptivity

of this device measured at normal incidence using unpolarized light was 99%. In the mid-IR at 6 μm, a MMA design composed of an array of nanoscale Au crosses on a planar alumina and Au thin film stack achieved a near-unity absorptivity of 97% at normal incidence.[22] In contrast, multiband MMAs require nanostructures with more sophisticated geometries to induce an additional electric and/or magnetic resonance for each absorption band, which forces additional restrictions on the design. Moreover, mechanically flexible constituent materials such as Kapton must be integrated to realize MMA coatings for curved surfaces. This added complexity has hindered progress in developing MMAs with highly customized multiband IR response to complement existing single-band[18,22] and broad-band absorbers.[24]

In this paper, we report on the electromagnetic design and nanofabrication of a conformal MMA optimized to have two nearly perfect, narrow absorption bands centered at mid-IR wavelengths of 3.3 and 3.9 μm. A genetic algorithm (GA) was used to identify an array of H-shaped nanoresonators on a flexible Kapton and Au thin film stack that excite the appropriate electric and magnetic resonances for strong absorption in each band. Measurements of a fabricated MMA are in strong agreement with theoretical predictions, showing polarization-independent absorptivity greater than 90% over a ±50° angular range in both of the targeted wavelength bands. Full-wave simulations that illuminate a curved metal surface protected with this conformal MMA coating confirm that nearly all of the reflected light is eliminated within the two absorption bands, which is in sharp contrast to the unprotected surface. This work represents a significant step toward realizing high-efficiency MMA coatings that suppress the reflection from curved surfaces at multiple bands within the 3 to 5 μm atmospheric window.

RESULTS AND DISCUSSION

Electromagnetic Design Optimization. Our dual-band mid-IR MMA employs a three-layer metallodielectric stack composed of two gold (Au) layers—a doubly periodic array of electrically isolated nanoresonators at the top and a solid ground plane at the bottom—separated by a thin dielectric layer. Kapton was chosen for our dielectric layer because it is a highly durable and flexible polymer that can easily conform to the topography of most practical curved surfaces. The array of Au nanostructures on the top screen creates a resonant electric response, while the Au ground plane functions together with the top screen to produce strong coupling to the magnetic component of the incident light. The continuous Au ground plane, which is thicker than the penetration depth of light in the mid-IR wavelength regime, prevents transmission of incident light through the structure. Therefore, strong absorption is achieved by minimizing the in-band reflection.

Importantly, the Au ground plane also decouples the electromagnetic properties of the MMA coating from the surface it protects, allowing integration onto curved surfaces of arbitrary materials.

The specific goal was to design a periodic array of nanoresonators that gives two polarization-independent absorption bands centered at 3.3 μm (90 THz) and 3.9 μm (77 THz) with absorptivity greater than 90%, i.e., at least 10 dB attenuation, over a ±50° field-of-view. The two closely spaced absorption band wavelengths were selected arbitrarily within the 3 to 5 μm atmospheric window for this proof-of-concept design. To achieve such dual-band performance using the described three-layer structure, a robust GA[25] coupled with a full-wave electromagnetic solver was employed to optimize the geometry and dimensions of the structure to best satisfy the user-defined requirements. For each of the starting candidate nanoresonator designs, the unit cell of the periodically patterned top Au layer was divided into a 14 × 14 grid of pixels that were randomly assigned a binary value corresponding to the presence "1" or absence "0" of Au on the pixel. The Au pattern was further constrained to possess 8-fold symmetry to achieve a polarization-independent absorber response. During the optimization, the unit cell size and the Kapton thickness were allowed to take values over a predefined range up to a maximum value of λ/2 to suppress higher order diffraction. To accurately account for the material dispersion in the design, the measured optical constants of the Au and Kapton thin film were used in the optimization. Furthermore, nanofabrication design constraints were incorporated to ensure that the optimized structure could be easily fabricated without modifying the nanoresonator geometry.[26,27]

During the GA evolution, the wavelength-dependent scattering parameters of each candidate design was calculated using the Ansoft High Frequency Structure Simulator (HFSS) full-wave finite-element solver with appropriate boundary conditions assigned to approximate a TEM wave incident on the structure at different angles. The absorptivity was calculated by $A_{TE,TM} = 1 - T_{TE,TM} - R_{TE,TM}$, where $R_{TE,TM} = |S_{11}|^2$ and $T_{TE,TM} = |S_{21}|^2$ represent the TE and TM reflectivity and transmittance, respectively. The absorptivity was evaluated against an ideal dual-band absorber response to determine its cost, given by

$$\text{cost} = \sum_\lambda \sum_{\theta_i} [(1 - A_{\theta_i, TE}) + (1 - A_{\theta_i, TM})] \quad (1)$$

where λ is the wavelength of the target bands (3.3 μm, 3.9 μm) and θ_i is the desired angle of incidence range (0° to 50°). The GA evolved the top Au screen nanoresonator geometry, unit cell size, and Kapton thickness until it converged to a sufficiently low-cost solution, i.e., the optimized design was achieved.

Nanoresonator Array for Dual-Band Absorption. The diagram of the GA-optimized dual-band MMA design is displayed
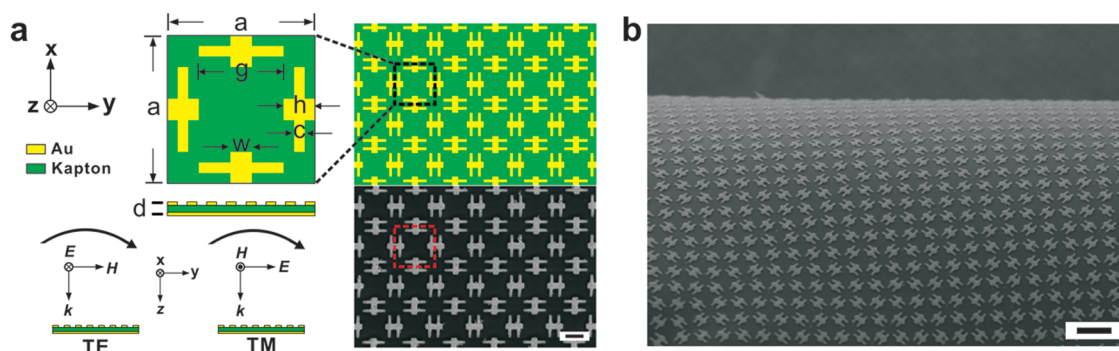
Figure 1. Diagram and FESEM image of the fabricated dual-band mid-IR MMA coating. (a) Top: Doubly periodic array of H-shaped nanoresonators showing magnified view of one unit cell with dimensions $a = 1475$ nm, $h = 315$ nm, $w = 210$ nm, $g = 840$ nm, $c = 105$ nm, and $d = 200$ nm (top and bottom Au: 50 nm, Kapton: 100 nm). **Bottom right:** FESEM image of a portion of the fabricated MMA. Scale = 600 nm. **Bottom left:** The orientation of the incident fields with respect to the MMA. **(b)** Low-magnification FESEM image of the freestanding fabricated conformal MMA coating showing its mechanical flexibility. Scale = 1800 nm.

in Figure 1a (top right). A detailed single unit cell illustration is shown in Figure 1a (top left), including its geometry and dimensions. The top Au screen is made up of a doubly periodic array of orthogonal stub-loaded H-shaped (SLH) nanoresonators identified by the GA, which have a central connecting bar that is 630 nm long and 210 nm wide and two arms that are 840 nm long and 105 nm wide. Each arm is offset from the edge of the central bar by 105 nm, and the arms are separated from one another by 210 nm. The total thickness of the three-layer structure is 200 nm, less than 1/15 of the operating wavelength. The orientations of the incident TE and TM polarized fields with respect to the MMA are illustrated in Figure 1a (bottom left). This design satisfies the nanofabrication design constraints imposed during design optimization, which ensures that the exact structure can be realized experimentally to minimize discrepancies that would degrade the resonant electromagnetic properties compared to theory.

The simulated reflectivity of the dual-band MMA at normal incidence as a function of wavelength is shown in Figure 2a for both polarizations. Transmission (not shown) is zero due to the Au ground plane. Two strong absorption bands are clearly resolved at the target wavelengths of 3.3 and 3.9 μm. Both bands have a -10 dB bandwidth of $\sim$0.1 μm with a maximum absorptivity of 94.7% or -0.24 dB (reflectivity of 6.3% and -12 dB) at 3.3 μm and of 99.6% or -0.02 dB (reflectivity of 0.4% and -24 dB) at 3.9 μm. Additional reflectivity data simulated at oblique incidence are plotted in Supporting Information, S1 and S2. The calculated angular dispersion of the absorption for both polarizations is shown in Figure 2b. The two vertical red strips demonstrate that the two absorption peaks remain centered at 3.3 and 3.9 μm over a broad range of incidence angles for both polarizations. The absorptivity in both bands remains >91% over a wide field-of-view of $\pm50°$ due to the efficient excitation of both electric and magnetic resonances. Further investigation shows that this MMA still achieves absorptivity of >60% for TE polarization and >85% for TM polarization in both

bands at an incident full angle of 160° (see Supporting Information, S2). Moreover, in the course of design optimization, we observed a design trade-off between the absorbing efficiency and the desired number of absorption bands, which is similar to the findings in other studies.[28−30] In spite of these trade-offs, the optimized dual-band MMA coating achieves all of the original performance goals.

Resonant Electromagnetic Properties. To understand the contribution of each H-shaped Au nanoresonator segment to the electric and magnetic response, the current distributions of the MMA at the center wavelength in each absorption band under a normally incident illumination with the electric-field linearly polarized in the x-direction are shown in Figure 3. For the first absorption band at 3.3 μm, the currents are primarily concentrated on the two arms of the SLH nanoresonator and the corresponding area of the ground plane underneath the arms (see Figure 3a). Similar to the so-called fishnet[31] and paired nanorod[32] structures, the antiparallel currents give rise to a magnetic resonance. In this band, the strength of the magnetic resonance overwhelms the electric response, and thus the strong absorption can be attributed to the nearly pure magnetic response of the structure. This dominant magnetic response indicates that an artificial magnetic conducting (AMC) condition[33] is satisfied, as confirmed by the zero reflection phase (see Supporting Information, S3) that is maintained regardless of the angle of incidence. For the second band at 3.9 μm, the current is mainly confined on the top Au layer and is concentrated in the connecting bar and the two arms of the SLH nanostructures, which behave as electric LC resonators (see Figure 3b). The inductance is introduced by the middle connecting bar, while the gaps between the two arms provide the capacitance. Therefore, the electric resonance is driven when the incident electric field is parallel to the arms. In addition, a magnetic resonance is also introduced by the antiparallel currents on the connecting bar and the corresponding area on the bottom Au ground plane. The
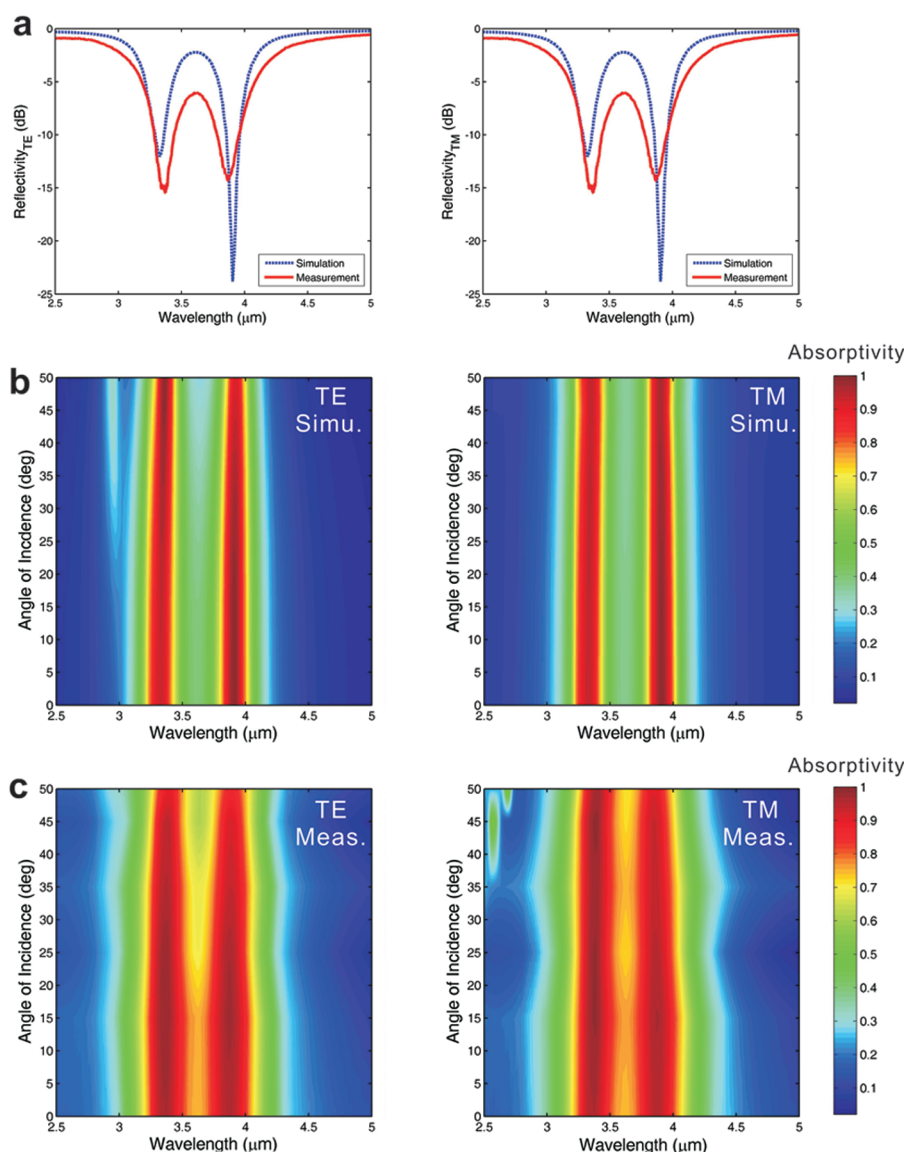
Figure 2. Angular peak dispersion of the MMA absorption spectra. (a) Simulated and measured reflectivity of the MMA coating under TE (left) and TM (right) illumination at normal incidence. The identical reflectivity is attributed to the 8-fold symmetry of the unit cell that enables the response of the structure to be independent of the azimuthal angle of the incoming light. **(b)** Contour plot of the simulated absorptivity as a function of wavelength and angle of incidence under TE (left) and TM (right) illumination. The two vertical red strips clearly show two strong absorption bands almost independent of the incident angle. **(c)** Contour plot of the measured absorptivity as a function of wavelength and angle of incidence under TE (left) and TM (right) illumination. The two angularly independent absorption bands agree well with the theoretical predictions. Near-unity absorptivities were achieved in both bands experimentally, confirming a successful realization of the designed structure.

combined contribution of both of these electric and magnetic resonances produces the strong absorption at 3.9 μm, consistent with the $-90°$ reflection phase that is shown in Supporting Information, S3.

Nanofabrication and Characterization. The GA-optimized MMA coating was fabricated by evaporating the Au ground plane layer and spin coating the thin Kapton dielectric layer on a handle substrate. The periodic array of H-shaped nanoresonators was patterned on top of the Kapton layer using electron beam lithography followed by a Au lift-off procedure, as shown in the field emission scanning electron microscope (FESEM) image in Figure 1a (bottom right). The three-layer

metallodielectric structure was then removed from the handle substrate to demonstrate its mechanical flexibility and durability (see Figure 1b). The reflectivity of the fabricated MMA at normal incidence, measured using a Fourier transform IR (FTIR) spectrometer (see Methods for detailed description of measurement setup), is shown in Figure 2a. The wavelengths corresponding to the maximum normal incidence reflectivity shifted by less than 3% from the simulated values, changing from 3.30 to 3.40 μm in the first band and from 3.90 to 3.85 μm in the second band. At these wavelengths, the measured reflectivity for both polarizations was 3.2% (-15 dB) and 4.0% (-14 dB),
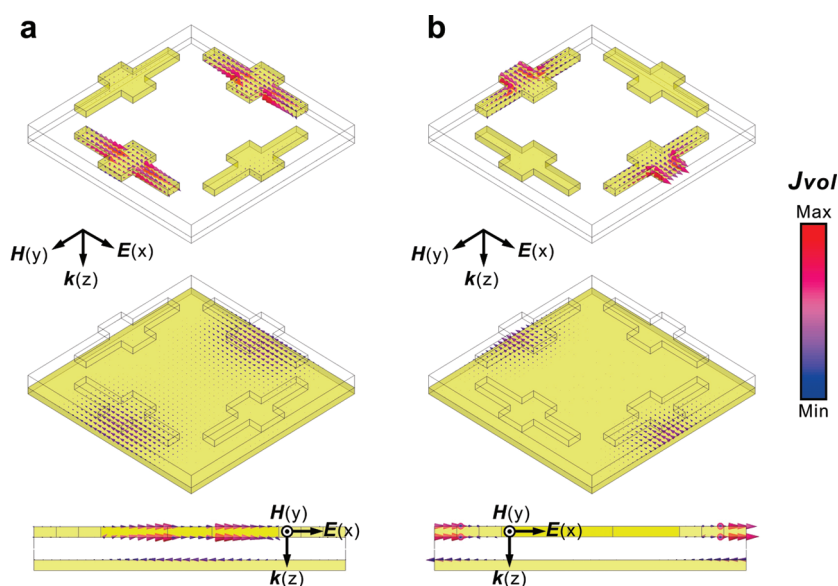
Figure 3. Finite-element method simulations of the unit cell current distributions at normal incidence. (a) 3D view of the current distribution in the top Au nanoresonator layer (top) and bottom Au ground plane layer (middle) for the first absorption band at 3.3 μm. The bottom plot shows the cross-sectional view of the current distribution. (b) 3D view of the current distribution in the top Au nanoresonator layer (top) and bottom Au ground plane layer (middle) for the second absorption band at 3.9 μm. The bottom plot shows the cross-sectional view of the current distribution.

respectively. This represents a decrease in reflectivity from 6.3% to 3.2% (3.1% difference) in the first band and an increase from 0.4% to 4.0% (3.6% difference) in the second band. Additional reflectivity data measured at oblique incidence can be found in the Supporting Information, S4. The absorptivity of the fabricated MMA, calculated from the measured reflectivity, is shown in Figure 2c as a function of both the wavelength and the angle of incidence. The two absorption peaks of the MMA remain above 90% for an incidence angle up to 50° for both polarizations, with the −10 dB bandwidth of both bands exhibiting a maximum broadening of 0.06 μm over the entire angular range compared to the simulated results.

The measured results confirm that the optical properties of the nanofabricated MMA coating agree well with the simulations for all of the initial design parameters. The sources of the small differences between experiment and theory were identified through an in-depth study of the fabricated structures by FESEM. Simulations reveal that the primary cause of the wavelength shift is the slight rounding at the ends of the patterned Au nanoresonators, which changes the effective electrical length of the central connecting bar and the two arms. Two primary factors contribute to the degradation in bandwidth. First, the slightly tapered sidewall profile (∼80°) of the evaporated Au nanoresonators results in some degradation in the quality factor of the resonances. Second, variations in the Au nanoresonator dimensions across the large-area MMA (∼5%) can give slightly shifted absorption bands, resulting in a broadened integrated line shape of the absorption peaks from the large-area structure.

Further optimization of the Au nanoresonator fabrication processes is expected to produce MMA coatings with even better correspondence to theory.

Protecting a Curved Surface with a MMA Coating. To investigate the performance of this conformal dual-band MMA for applications such as mid-IR reflection suppression, we conducted a 3D full-wave simulation of the MMA coating a curved metal surface. As the schematics in Figure 4a,b illustrate, the field pattern of a curved Au ground plane is compared with that of the same ground plane protected by the MMA when illuminated by an obliquely incident beam with a finite beamwidth. The insets show the 3D views of the structures for each case. Without the MMA coating, the curved ground plane creates strong reflections in multiple directions for each band, as shown in Figure 4c. The field snapshots show that standing wave patterns arise due to the interference between the incident and reflected waves. However, when the MMA covers the curved surface, reflection is nearly eliminated for both polarizations in both bands, as displayed in Figure 4d,e. A slight reflection remains near the horizon, which is caused by the portion of the curved MMA that is illuminated by waves at near-grazing incidence angles. This can be attributed to the reduction in absorptivity that occurs at large incidence angles, particularly for the TE polarization (see Figure S2). Field animations are available in the Supporting Information, S5. The considerable reduction in reflection achieved by the MMA coating confirms that its performance is retained when it protects a highly reflective curved surface. In addition, as is evident from Figure 4d,e, the field is strongly confined
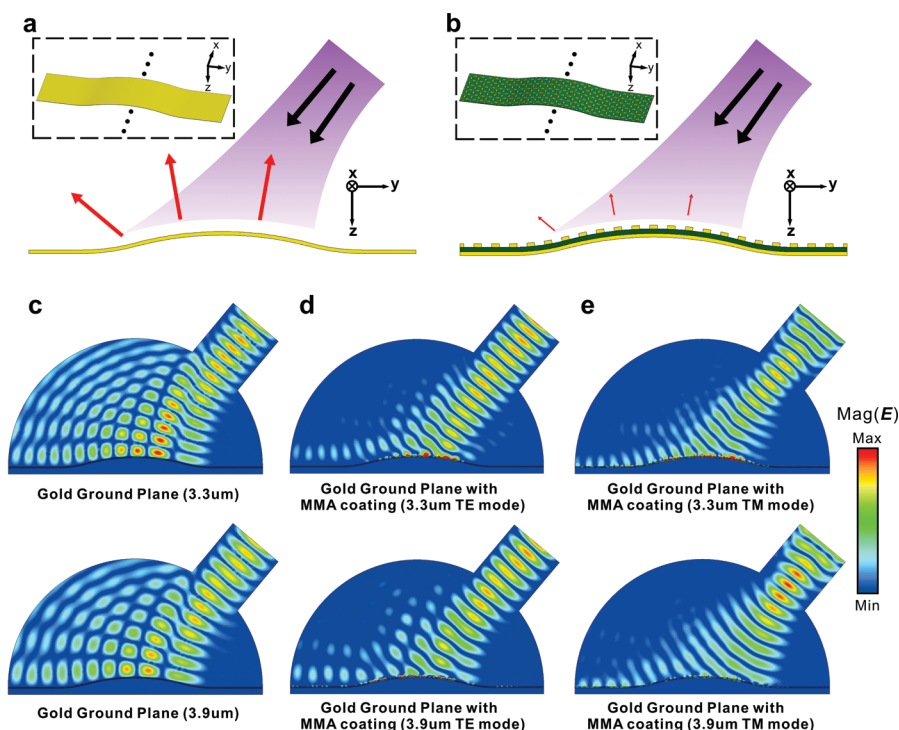
Figure 4. Finite-element method simulations of curved metal surface protected with a MMA coating. (a) Schematic of an unprotected curved metal surface (50 nm Au) producing strong reflection in multiple directions when illuminated by an incident beam. The inset shows a 3D view of the curved metal surface. **(b)** Schematic of a MMA-coated curved metal surface (50 nm Au) with significantly reduced reflection when illuminated by an incident beam. The inset shows a 3D view of the MMA-coated curved metal surface. **(c)** Simulation of the electric field magnitude for the unprotected curved metal surface at 3.3 μm (top) and 3.9 μm (bottom). **(d)** Simulation of the electric field magnitude for the MMA-coated curved metal surface under TE incident illumination at 3.3 μm (top) and 3.9 μm (bottom). **(e)** Simulation of the electric field magnitude for the MMA-coated curved metal surface under TM incident illumination at 3.3 μm (top) and 3.9 μm (bottom).

within the thin functional layer (only $\sim 1/15\lambda$) of the MMA, indicating a high absorptivity-over-thickness efficiency that is superior to conventional (nonmetamaterial) absorbers. Moreover, no fields are observed behind the solid Au ground plane; accordingly, the performance will not be affected by the object that the MMA covers, making it useful as a coating on various metal and dielectric surfaces.

CONCLUSIONS

In conclusion, we have shown the design and nanofabrication of a polarization-insensitive, dual-band MMA with measured absorptivity greater than 90% over a $\pm 50°$ incidence-angle range in the mid-IR

at 3.3 and 3.9 μm. Electromagnetic simulations confirm that the absorption properties of the metamaterial are due to the electric and/or magnetic resonances excited by the periodic array of H-shaped nanoresonators patterned on a Kapton and Au thin film stack in both wavelength bands. The highly conformal nature of the MMA coating was demonstrated experimentally, and 3D full-wave simulations show that the absorbing properties are maintained when it is placed on a highly reflective curved surface. Because the performance of the MMA is independent of the material it protects, it is promising for a variety of applications, including suppressing the mid-IR reflection of curved metal surfaces in more than one wavelength band.

METHODS

Nanofabrication Process Flow and Mid-IR Measurement. Nanofabrication of the GA-optimized MMA began by thermally evaporating a 50 nm gold layer on a clean Si wafer. The intermediate Kapton layer was then deposited on top of this bottom gold layer by spin coating the wafer with the polyimide precursor (HD Microsystems PI2556:T9039 = 1:2). The as-spun polyimide film was soft baked at 120 °C for one minute and then cured in a N$_2$-purged convection oven at 250 °C for one hour in order to complete the imidization through elimination of the solvent. The top Au nanoresonator array was defined using electron-beam lithography and a metal lift-off process. A layer of

electron-beam resist (Nippon ZEP 520A) was spun onto the Kapton layer. After exposing (Leica EBPG-5HR) and developing the pattern, a 50 nm Au film was evaporated and lifted-off by dissolving the resist (MicroChem NANO REMOVER PG).

The MMA reflectivity was measured using a Fourier transform IR spectrometer (Bruker Optics IFS-66 main compartment) equipped with a liquid nitrogen cooled mercury cadmium telluride (MCT) detector. For near-normal incidence (<1° off normal) measurements, a custom optical setup composed of mirrors and a beam splitter was constructed in the main sample compartment of the FTIR to direct the reflected IR signal to the MCT detector. For oblique incidence measurements, the sample

was mounted on a variable-angle specular reflection accessory (Thermo Spectra-Tech model 500) to collect the angle-resolved reflectivity data in 10° increments to a maximum angle of 50°. In each case, the absolute reflectivity was determined by referencing the measured values to the reflectivity of a Au mirror. The contour plot in Figure 2c was generated by linear interpolation between the measured reflectivity values.

Metamaterial Absorber Coated Curved Metal Surface Simulation. For the simulation of the MMA-coated curved metal ground plane surface, the HFSS finite element solver was employed. In the simulation domain, a strip of the MMA with a width of one unit cell in the *x* direction and a length of 26 unit cells was considered. To mimic a 1D infinite structure, perfect electric conducting boundary conditions were assigned to the front and back walls in the *x* direction for TE polarization and perfect magnetic conducting boundary conditions for TM polarization. A waveguide was connected to the semicircular air box as a feed for a finite width beam impinging obliquely on the structure. Dispersive optical constants measured by variable-angle spectroscopic ellipsometry were also included to accurately model the Au and Kapton layers.

Supporting Information Available: Additional simulated and measured MMA reflectivity results (S1−S3). Additional measured MMA reflectivity results (S4). Animation of simulated field distribution of curved surface coating application (S5). This material is available free of charge *via* the Internet at http://pubs.acs.org.

REFERENCES AND NOTES

1. Cai, W.; Shalaev, V. *Optical Metamaterials: Fundamental and Applications*; Springer, New York, 2010.
2. Shalaev, V. Optical Negative-Index Metamaterials. *Nat. Photonics* **2007,** *1*, 41–48.
3. Pendry, J. B. Negative Refraction Makes a Perfect Lens. *Phys. Rev. Lett.* **1999,** *85*, 3966–3969.
4. Zhang, X.; Liu, Z. Superlenses to Overcome the Diffraction Limit. *Nat. Mater.* **2008,** *7*, 435–441.
5. Kwon, D.-H.; Werner, D. H. Transformation Optical Designs for Wave Collimators, Flat Lenses and Right-Angle Bends. *New J. Phys.* **2008,** *10*, 115023.
6. Pendry, J. B.; Schurig, D.; Smith, D. R. Controlling Electromagnetic Fields. *Science* **2006,** *312*, 1780–1782.
7. Valentine, J.; Li, J.; Zhang, S.; Zentgraf, T.; Bartal, G.; Zhang, X. An Optical Cloak Made of Dielectrics. *Nat. Mater.* **2009,** *8*, 568–571.
8. Landy, N. I.; Sajuyigbe, S.; Mock, J. J.; Smith, D. R.; Padilla, W. J. A Perfect Metamaterial Absorber. *Phys. Rev. Lett.* **2008,** *100*, 207402.
9. Kern, D. J.; Werner, D. H. A Genetic Algorithm Approach to the Design of Ultra-Thin Electromagnetic Bandgap Absorbers. *Micro-Opt. Technol. Lett.* **2003,** *38*, 61–64.
10. Wang, B.; Koschny, T.; Soukoulis, C. M. Wide-Angle and Polarization-Independent Chiral Metamaterial Absorber. *Phys. Rev. B* **2009,** *80*, 033108.
11. Cheng, Q.; Cui, T. J.; Jiang, W. X.; Cai, B. G. An Omnidirectional Electromagnetic Absorber Made of Metamaterials. *New J. Phys.* **2010,** *12*, 063006.
12. Tao, H.; Bingham, C. M.; Strikwerda, A. C.; Pilon, D.; Shrekenhamer, D.; Landy, N. I.; Fan, K.; Zhang, X.; Padilla, W. J.; Averitt, R. D. Highly Flexible Wide Angle of Incidence Terahertz Metamaterial Absorbers: Design, Fabrication, and Characterization. *Phys. Rev. B* **2008,** *78*, 241103.
13. Zhu, W.; Zhao, X. Metamaterial Absorber with Dendritic Cells at Infrared Frequencies. *J. Opt. Soc. Am. B* **2009,** *26*, 2382–2385.
14. Wen, Q.-Y.; Zhang, H.-W.; Xie, Y.-S.; Yang, Q.-H.; Liu, Y.-L. Dual Band Terahertz Metamaterial Absorber: Design, Fabrication, and Characterization. *Appl. Phys. Lett.* **2009,** *95*, 241111.
15. Tao, H.; Bingham, C. M.; Pilon, D.; Fan, K.; Strikwerda, A. C.; Shrekenhamer, D.; Padilla, W. J.; Zhang, X.; Averitt, R. D. A Dual Band Terahertz Metamaterial Absorber. *J. Phys. D: Appl. Phys.* **2010,** *43*, 225102.
16. Bingham, C. M.; Tao, H.; Liu, X.; Averitt, R. D.; Zhang, X.; Padilla, W. J. Planar Wallpaper Group Metamaterials for Novel Terahertz Applications. *Opt. Express* **2008,** *16*, 18565–18575.
17. Tao, H.; Landy, N. I.; Bingham, C. M.; Zhang, X.; Averitt, R. D.; Padilla, W. J. A Metamaterial Absorber for the Terahertz Regime: Design, Fabrication and Characterization. *Opt. Express* **2008,** *16*, 7181–7188.
18. Liu., N.; Mesch, M.; Weiss, T.; Hentschel, M.; Giessen, H. Infrared Perfect Absorber and Its Application as Plasmonic Sensor. *Nano Lett.* **2010,** *10*, 2342–2348.
19. Cubukcu, E.; Zhang, S.; Park, Y.-S.; Bartal, G.; Zhang, X. Split Ring Resonator Sensors for Infrared Detection of Single Molecular Monolayers. *Appl. Phys. Lett.* **2009,** *95*, 043113.
20. Diem, M.; Koschny, T.; Soukoulis, C. M. Wide-Angle Perfect Absorber/Thermal Emitter in the Terahertz Regime. *Phys. Rev. B* **2009,** *79*, 033101.
21. Landy, N. I.; Bingham, C. M.; Tyler, T.; Jokerst, N.; Smith, D. R.; Padilla, W. J. Design, Theory, and Measurement of Polarization-Insensitive Absorber for Terahertz Imaging. *Phys. Rev. B* **2009,** *79*, 125104.
22. Liu, X.; Starr, T.; Starr, A. F.; Padilla, W. J. Infrared Spatial and Frequency Selective Metamaterial with Near-Unity Absorbance. *Phys. Rev. Lett.* **2010,** *104*, 207403.
23. Kown, D.-H.; Werner, D. H. Transformation Electromagnetics: An Overview of the Theory and Applications. *IEEE Antennas Propag. Mag.* **2010,** *52*, 24–46.
24. Han, S. W.; Park, Y. S.; Neikirk, D. P. Broadband Infrared Detection Using Jaumann Absorbers with Genetic Algorithm. *Electron. Lett.* **2005,** *41*, 1307–1308.
25. Haupt, R. L.; Werner, D. H. *Genetic Algorithms in Electromagnetics*; Wiley: Hoboken, NJ, 2007.
26. Tang, Y.; Bossard, J. A.; Werner, D. H.; Mayer, T. S. Single-Layer Metallodielectric Nanostructures as Dual-Band Midinfrared Filters. *Appl. Phys. Lett.* **2008,** *92*, 263106.
27. Yun, S.; Bossard, J. A.; Mayer, T. S.; Werner, D. H. Angle and Polarization Tolerant Midinfrared Dielectric Filter Designed by Genetic Algorithm Optimization. *Appl. Phys. Lett.* **2010,** *96*, 223101.
28. Through comparison of the performance among optimized single-band, dual-band, and triple-band absorbers, we found that by increasing the number of absorption bands, the angular performance is degraded, *i.e.*, a smaller field-of-view.
29. Navarro-Cía, M.; Beruete, M.; Agrafiotis, S.; Falcone, F.; Sorolla, M.; Maier, S. A. Broadband Spoof Plasmonics and Subwavelength Electromagnetic Energy Confinement on Ultrathin Metafilms. *Opt. Express* **2009,** *17*, 18184–18195.
30. Williams, C. R.; Misra, M.; Andrews, S. R.; Maier, S. A.; Carretero-Palacios, S.; Rodrigo, S. G.; Garcia-Vidal, F. J.; Martin-Moreno, L. Dual Band Terahertz Waveguiding on a Planar Metal Surface Patterned with Annual Holes. *Appl. Phys. Lett.* **2010,** *96*, 011101.
31. Zhang, S.; Fan, W.; Panoiu, N. C.; Malloy, K. J.; Osgood, R. M.; Brueck, S. R. Experimental Demonstration of Near-Infrared Negative-Index Metamaterials. *Phys. Rev. Lett.* **2005,** *95*, 137404.
32. Shalaev, V. M.; Cai, W.; Chettiar, U. K.; Yuan, H.-K.; Sarychev, A. K.; Drachev, V. P.; Kildishev, A. V. Negative Index of Refraction in Optical Metamaterials. *Opt. Lett.* **2005,** *30*, 3356–3358.
33. Sievenpiper, D.; Zhang, L.; Broas, R. F.; Alexopolous, N. G.; Yablonovitch, E. High-Impedance Electromagnetic Surfaces with a Forbidden Frequency Band. *IEEE Trans. Microwave Theory* **1999,** *47*, 2059–2074.